MATERIALS SCIENCE

Tissue-like skin-device interface for wearable bioelectronics by using ultrasoft, mass-permeable, and low-impedance hydrogels

Chanhyuk Lim[1,2†], Yongseok Joseph Hong[1,2†], Jaebong Jung[3†], Yoonsoo Shin[1,2], Sung-Hyuk Sunwoo[1,2], Seungmin Baik[1,2], Ok Kyu Park[1,4], Sueng Hong Choi[1,4], Taeghwan Hyeon[1,2], Ji Hoon Kim[3]*, Sangkyu Lee[1]*, Dae-Hyeong Kim[1,2,5]*

Hydrogels consist of a cross-linked porous polymer network and water molecules occupying the interspace between the polymer chains. Therefore, hydrogels are soft and moisturized, with mechanical structures and physical properties similar to those of human tissue. Such hydrogels have a potential to turn the microscale gap between wearable devices and human skin into a tissue-like space. Here, we present material and device strategies to form a tissue-like, quasi-solid interface between wearable bioelectronics and human skin. The key material is an ultrathin type of functionalized hydrogel that shows unusual features of high mass-permeability and low impedance. The functionalized hydrogel acted as a liquid electrolyte on the skin and formed an extremely conformal and low-impedance interface for wearable electrochemical biosensors and electrical stimulators. Furthermore, its porous structure and ultrathin thickness facilitated the efficient transport of target molecules through the interface. Therefore, this functionalized hydrogel can maximize the performance of various wearable bioelectronics.

INTRODUCTION

Transcutaneous bioanalysis and therapy, such as local oxygen concentration measurement (*1*), impedance sensing (*2*), drug delivery (*3*), and electrical stimulation (*4*), are commonly conducted in clinics. However, conventional devices for transcutaneous biosensing and treatment are generally not suitable for point-of-care–type applications, such as wearable bioelectronics, as they typically include a hard housing to store liquid electrolytes and accompany bulky electrochemical biosensing machines or drug delivery systems. These features of the conventional devices limit their applications in next-generation personalized medicine, which aims for real-time ubiquitous health monitoring and customized feedback treatment.

As an alternative to the conventional rigid and bulky devices, ultrathin flexible devices on polymeric substrates have been proposed (*5*–*9*). These include biosensing devices that detect biosignals and/or biomarkers on human skin to gather physiological or biochemical information (*10*–*21*) and drug delivery devices that supply feedback therapies (*22*–*25*). The ultrathin form factor of these devices reduces flexural rigidity and thus prevents mechanical failure when the device is deformed upon human movement (*26*). Despite the promising potential of flexible biomedical devices, there are several challenges. One critical issue is that the skin has microscale wrinkles, and typical wearable devices based on polymer films cannot perfectly follow the microscopic curvature of these wrinkles (*27*). This induces microscale air pockets between the flexible device and the skin, prohibiting the formation of ideal electrical/physical contacts and limiting the precise monitoring of biosignals (*23*, *28*) and efficient delivery of drug molecules (*29*). In addition, these flexible devices cannot efficiently carry liquid-state ionic molecules, such as electrolytes and drugs.

Hydrogels—cross-linked polymeric networks that contain a large volume of water within the porous structure (*30*, *31*)—have long been used in biomedical applications (*32*–*36*). The polymeric network imparts properties of a solid to hydrogels as they can be easily molded and structured into various shapes, while the high water content allows them to exhibit liquid-like characteristics. Thus, hydrogels have a potential to replace hard housings and liquid electrolytes of conventional transcutaneous biosensing devices. Furthermore, its soft and moisturized nature can help form extremely conformal contacts with the rugged skin surface, while the porous hydrogel structure allows for the facile transport of molecules. Therefore, a properly functionalized and processed form of hydrogels can have mechanical (soft), chemical (moisturized), and physical (permeable) properties similar to human tissue.

We here propose a skin-device interface with tissue-like features, formed by using an ultrathin type of a functionalized hydrogel. The functionalized hydrogel film is based on poly(acrylamide) (PAAm), which can form a stationary quasi-solid but moisturized interface between the wearable bioelectronic device and human skin (fig. S1A). Its ultrasoft mechanical property allows for conformal contacts with the corrugated skin surface (fig. S1B). Moreover, the highly porous three-dimensional (3D) network and the ultrathin thickness of the interfacing hydrogel enable the rapid diffusion and transport of target bioanalytes or drug molecules, which are important for transcutaneous bioanalysis and therapy (fig. S1Ci). In addition, the hydrogel functionalized with conductive polymers exhibits low impedance, which is beneficial for impedance sensing or electrical stimulation (fig. S1Cii). Using this ultrathin, functionalized hydrogel with high mass-permeability and low impedance, we were able to develop high performance wearable bioelectronic devices, such as a

[1]Center for Nanoparticle Research, Institute for Basic Science (IBS), Seoul 08826, Republic of Korea. [2]School of Chemical and Biological Engineering, Institute of Chemical Processes, Seoul National University, Seoul 08826, Republic of Korea. [3]School of Mechanical Engineering, Pusan National University, Busan 46241, Republic of Korea. [4]Department of Radiology, Seoul National University College of Medicine, Seoul 03080, Republic of Korea. [5]Department of Materials Science and Engineering, Seoul National University, Seoul 08826, Republic of Korea.
*Corresponding author. Email: dkim98@snu.ac.kr (D.-H.K.); sangkyulee@snu.ac.kr (S.L.); kimjh@pusan.ac.kr (J.H.K.)
†These authors contributed equally to this work.

transcutaneous oxygen pressure ($tcPO_2$) sensor, an impedance sensor, an iontophoretic drug delivery device, and a transcutaneous electrical nerve stimulator (TENS), for transcutaneous bioanalysis and therapy.

RESULTS

Ultrasoft, mass-permeable, and low-impedance hydrogel for a tissue-like skin-device interface

Flexible polyimide (PI) films (typical thickness of 1 to 25 μm; fig. S2A, left) are representative substrates for skin-mountable devices (*25*, *37*, *38*). Although they form a more conformal contact with the skin than do conventional rigid devices, a small layer of air pockets is still formed between the PI film and the skin surface as shown in the cross-sectional scanning electron microscopy (SEM) image (Fig. 1A); this is attributed to the microscale roughness of the human skin (fig. S2, B and C) (*27*). In contrast, PAAm hydrogels (fig. S2A, right) provided extremely conformal contacts with human skin due to their intrinsic softness (cf. Young's modulus of PI, PAAm hydrogel, and human skin: 2.5 GPa, 8 kPa, and 50 to 150 kPa, respectively (*39*–*41*)). The ultrasoft hydrogel film followed the microscale contour of the skin and left virtually no gaps at the interface (Fig. 1B).

Finite element analysis (FEA) was conducted to compare the contact of the PI and the hydrogel film on human skin. For the PI film, the linear elasticity model was used, whereas the incompressible neo-Hookean model was used for the hydrogel film and human skin. The simulation results supported the difference in the contact efficacy between the hydrogel (fig. S2D, top) and the conventional PI film (fig. S2D, bottom). Additional clarification on the mechanical simulation is provided in section S1.

An extremely conformal skin-device interface can be used for the wearable bioelectronics, such as devices for transcutaneous bioanalysis and therapy. However, instead of conventional high impedance and thick hydrogels, a novel type of hydrogel with further functionalization and a controlled thickness is required for the high-performance transcutaneous bioelectronics. Figure 1C briefly introduces the principle and requirements of the bioelectronics that can work through the tissue-like hydrogel interface. For example, an integrated wearable system for transcutaneous bioanalysis and therapy would consist of four types of representative device units, including a $tcPO_2$ sensor, a tissue impedance sensor, an iontophoretic drug delivery device, and a TENS.

For measuring $tcPO_2$, the oxygen molecules diffusing out from the heated skin surface must travel through the hydrogel and reach the electrode. For transdermal drug delivery, the ionic drugs loaded in the hydrogel need to be delivered to the tissue through the hydrogel. Therefore, these devices require the rapid transport of molecules via an ultrathin and mass-permeable hydrogel. For tissue impedance monitoring and transcutaneous electrical nerve stimulation, low impedance of the hydrogel is critical for sensitive and low-noise measurement as well as efficient charge injection into the skin. Therefore, lowering the impedance of a hydrogel is required, which can be achieved via functionalization with conductive polymers. The ultrathin functionalized hydrogel should meet these requirements, i.e., high mass-permeability, low impedance, and conformal contact with the skin.

Figure 1D shows an example of an integrated system equipped with an ultrathin, functionalized hydrogel for transcutaneous bioanalysis and therapy. The devices were fabricated on a flexible substrate, and then the ultrathin, functionalized hydrogels were integrated on the surface of these devices. Figure 1 (E and F) shows the mass-permeable hydrogel on the $tcPO_2$ sensor and the low-impedance hydrogel on the TENS electrode, respectively. The fabricated devices can be applied to any part of the skin for the aforementioned applications (Fig. 1G), and the ultrathin, functionalized hydrogel successfully forms a tissue-like skin-device interface.

Experimental and computational analysis of mass and heat transfer through the hydrogel interface

When the hydrogel interface is combined with wearable devices such as a $tcPO_2$ sensor or an iontophoretic drug delivery device, rapid diffusion of oxygen molecules or fast transport of drug ions through the hydrogel is important. To minimize the length of the mass transfer path, an ultrathin hydrogel (~150 μm) is preferred. To quantitatively study the effect of the hydrogel thickness on the mass transfer, computational analyses using the multiscale FEA method were performed.

On the basis of the SEM image of the hydrogel (Fig. 2A), Voronoi cells were formed by the simulation (Fig. 2B, left). Mass transfer through the moisturized hydrogel matrix is affected by the interconnected cellular structure of the hydrogel; however, the cellular model is not efficient for analyzing the effect of hydrogel thickness on diffusion in the case of thick hydrogels because of the large computational load (fig. S3, Ai and Bi). Instead, effective diffusivity can be determined from the cellular model of the thin hydrogel (150 μm) and then applied to a continuum model (Fig. 2B, right, fig. S3, Aii and Bii) for thick hydrogels (e.g., 500 and 1000 μm). The effective diffusivity was calculated from the average steady-state flux passing through surface A in the x direction j_x using the following equation

$$D_{\text{eff}} = -j_x \frac{\Delta c}{\Delta x} \tag{1}$$

where Δc and Δx are the concentration difference and the distance between surfaces, respectively. Next, a continuum media with a homogenized diffusivity was assumed for thick hydrogels (Fig. 2C).

The mass transfer of oxygen molecules and drug ions through the hydrogel matrix was also experimentally investigated for various hydrogel thicknesses, and experimental results were compared with the simulations (Fig. 2, D to G). To visualize the diffusion of drug ions through the hydrogel, rhodamine B dye was used as a model molecule because it ionizes in water and has a similar molecular weight to that of conventional drug molecules. The effective diffusivities of oxygen molecules and rhodamine B were calculated using Eq. 1. The models were discretized as eight-node linear hexahedral mass diffusion elements with an element size of 10 μm. The transient diffusion of both oxygen and rhodamine B dye molecules was calculated with following conditions: an initial concentration of zero and a surface concentration constant with solubility s.

First, the amount of penetrated oxygen molecules through the hydrogels was measured (Fig. 2D); the thinner the hydrogel was, the more oxygen molecules penetrated. The simulation showed that the thick hydrogel (1000 μm) retarded the diffusion of oxygen molecules significantly (Fig. 2E). Moreover, molecular diffusion through the thick hydrogel (>1500 s) required more time than diffusion through the thin hydrogel (190 s for the 150-μm film). In the case of rhodamine B, ionized molecules diffused into the hydrogel. When a designated amount of rhodamine B was applied onto the hydrogel, the dye reached a depth of 150 μm within 1 min (Fig. 2F). However, diffusion slowed down significantly in the deeper regions of the

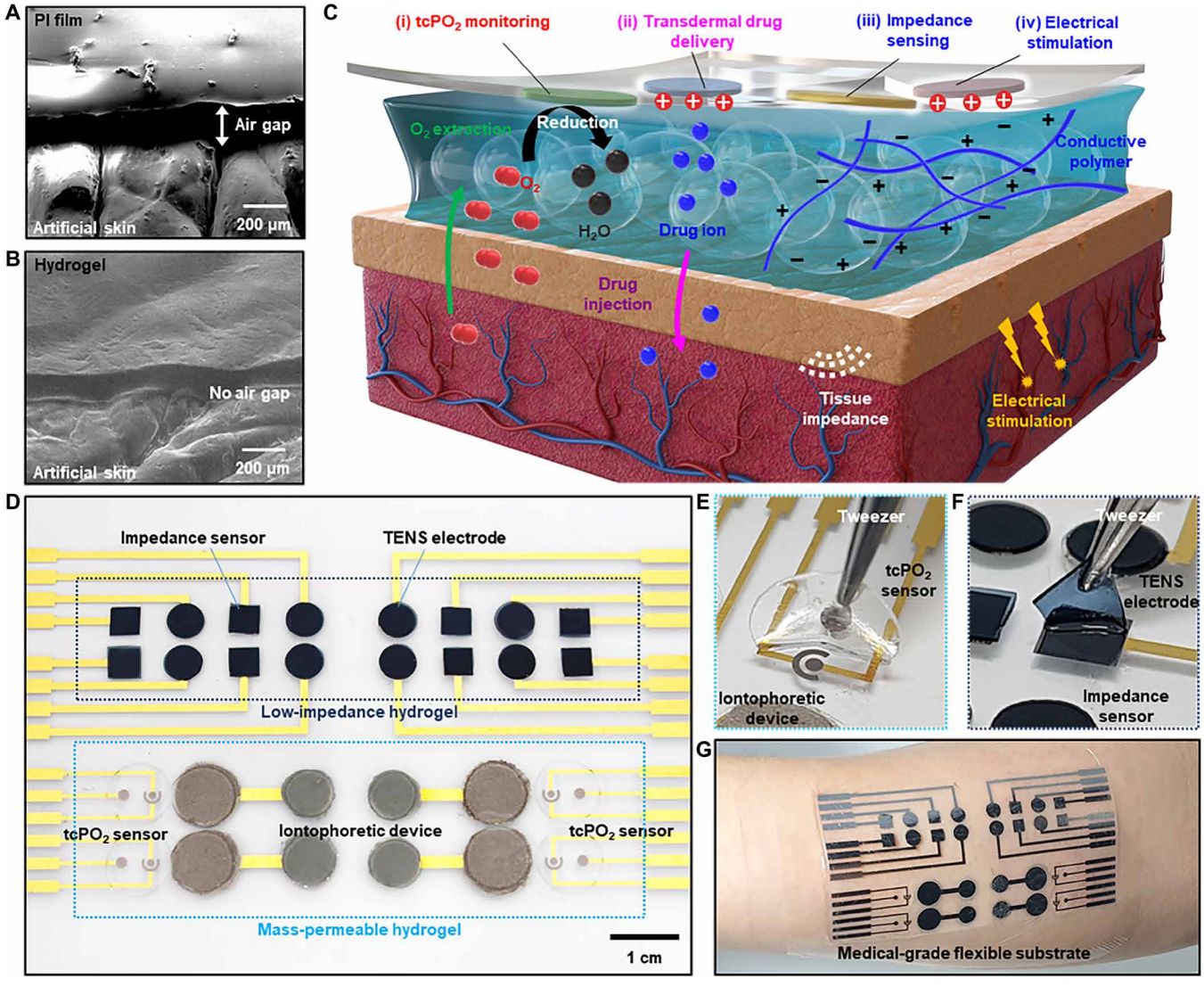

Fig. 1. Tissue-like skin-device interface obtained using an ultrasoft, mass-permeable, and low-impedance hydrogel. (**A** and **B**) Scanning electron microscopy (SEM) images of the PI film (A) and the tissue-like ultrasoft hydrogel (B) mounted on artificial skin. (**C**) Illustration of the structure, requirement, and roles of the hydrogel interface between human skin and the wearable bioelectronics. The exemplified wearable device is used for transcutaneous bioanalysis and therapy, such as $tcPO_2$ monitoring, transdermal drug delivery, tissue impedance sensing, and electrical stimulation. (**D**) Picture of the integrated wearable device on a flexible substrate. The system includes four representative types of devices for biosensing and therapy, and each device is integrated with the ultrathin functionalized hydrogel. (**E**) Picture of the mass-permeable hydrogel on the $tcPO_2$ sensor. (**F**) Picture of the low-impedance hydrogel on the TENS electrode. (**G**) Picture of the integrated device applied to human skin. Photo credits: (D to F) Yongseok Joseph Hong, Seoul National University and (G) Sangkyu Lee, Institute for Basic Science.

hydrogel because of the reduced concentration gradient. Simulation results also showed that delayed diffusion occurred in the thick hydrogel film (Fig. 2G). Further elaboration on the details and supplementary results of the mass transfer analysis can be found in section S2.

When the human skin is heated to ~43°C, oxygen molecules can be extracted from the blood vessels (*1*). Therefore, facile heat transfer, as well as mass transfer, through the hydrogel is important for $tcPO_2$ sensing. We thus examined heat transfer through hydrogels of different thicknesses. To experimentally determine the amount of heat transfer occurring, hydrogels with different thicknesses were placed on a plate preheated to 43°C, and their surface temperature was measured using an infrared (IR) camera (Fig. 2, H and I). Simulations were also carried out for comparison (Fig. 2J).

When the heating plate was covered with an ultrathin hydrogel (150 μm), the surface temperature of the hydrogel reached 43°C within 10 min (cf. 2 min for the bare plate to reach 43°C). In contrast, the target temperature (43°C) was not achieved within the timeframe of this study (15 min) when a thick hydrogel (1000 μm) covered the plate, as it hindered heat transfer. Next, the vertical temperature gradient inside the hydrogel was simulated for various hydrogel thicknesses (150, 300, 500, and 1000 μm); the temperature of the heat source in contact with the hydrogels was set to 45°C and the calculated steady-state temperatures were 44.5°, 43.8°, 42.8°, 41.6°, and 39.5°C for each hydrogel-skin interface, respectively (Fig. 2J). These analyses demonstrate the importance of using an ultrathin hydrogel. Note that the 60-μm-thick hydrogel film is expected to

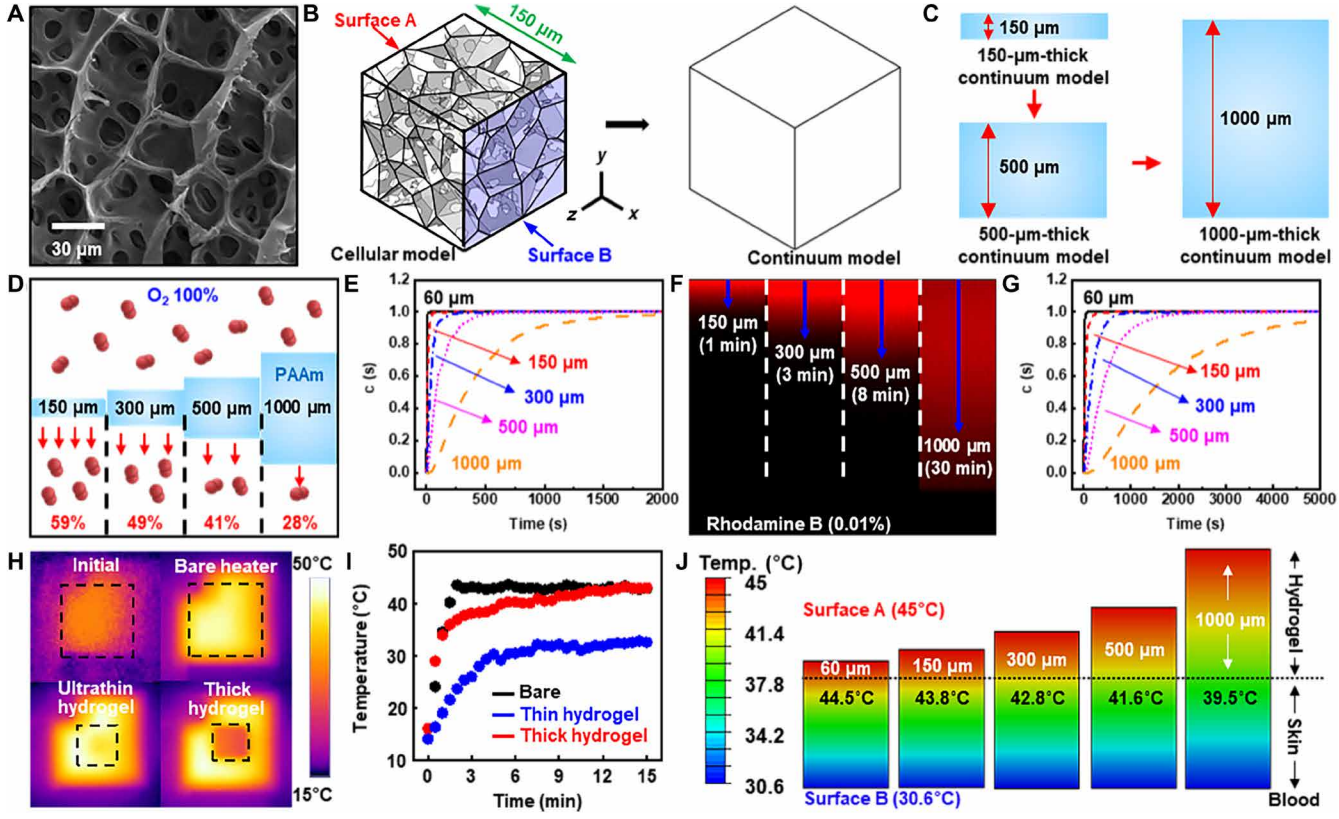

Fig. 2. Experimental and computational analysis of mass transfer and heat transfer through the hydrogel. (**A**) SEM image showing the cellular structure of the hydrogel. (**B**) Diagram illustrating the conversion of a Voronoi cell–based model into a continuum model. (**C**) Thick hydrogel model made from stacking a couple of thin hydrogel models. (**D**) Amount of oxygen penetrating hydrogels with various thicknesses. (**E**) Computational analysis of oxygen diffusion through hydrogels with various thicknesses. (**F**) Diffusion depths of rhodamine B dye into the hydrogel observed via confocal microscopy. (**G**) Computational analysis of the diffusion of drug ions into the hydrogel. (**H** and **I**) Infrared (IR) camera images (H) and temperature versus time plots (I) of a bare heated plate and heated plates covered with the thin (150 μm) and thick (1000 μm) hydrogels. (**J**) FEA of heat transfer through hydrogels with various thicknesses.

have higher performances than the 150-μm-thick hydrogel film. However, the 60-μm-thick hydrogel film can be easily torn during its handling. Future studies to improve the mechanical property of the hydrogel film are needed to use the 60-μm-thick hydrogel film. Detailed information on the simulation method for heat transfer analysis is included in section S3.

Synthesis and characterization of the low-impedance hydrogel

Another important feature of the tissue-like hydrogel interface is low-impedance. In this study, we used a PAAm hydrogel as the base material. PAAm hydrogels are typically synthesized by adding salts to PAAm precursors; however, this conventional PAAm results in high impedance (*42*), which reduces the signal-to-noise ratio of impedance sensing and the charge injection efficiency of the electrical stimulation. Therefore, a low-impedance hydrogel was synthesized by incorporating the conductive polymer poly(3,4-ethylenedioxythiophene): polystyrene sulfonate (PEDOT:PSS). PEDOT:PSS increases electrical conductivity (*43*, *44*), decreases impedance (*45*), and improves charge injection capability (*44*), making it useful for fabricating conductive hydrogels (*33*, *46*).

An aqueous solution of PEDOT:PSS (Fig. 3Ai) was freeze-dried to solidify PEDOT:PSS (Fig. 3Aii). Then, the solidified PEDOT:PSS was mixed with the PAAm precursor solution containing acrylamide (AAm; monomer), bis-acrylamide (cross-linker), and ammonium persulfate (APS; initiator) (Fig. 3Aiii). The prepared solution was poured into a glass mold to control its thickness, after which the mold was placed on a hot plate set to 90°C for 15 min to obtain a solidified film (Fig. 3Aiv). During this process, the PEDOT:PSS particles can be distributed inside the PAAm hydrogel matrix, which forms a PEDOT:PSS/PAAm hydrogel (Fig. 3B).

Fourier transform–IR (FT-IR) spectroscopy analysis confirmed the successful synthesis of the PEDOT:PSS/PAAm hydrogel (Fig. 3, C and D), which—compared with the bare PAAm hydrogel (Fig. 3C)—had additional peaks derived from the $-SO_3$ functional group of PEDOT:PSS (Fig. 3D) (*47*). More detailed FT-IR data are shown in fig. S4. Energy dispersive x-ray spectroscopy (EDS) analysis also confirmed the homogeneous distribution of PEDOT:PSS chains within the hydrogel matrix (fig. S5). The microporous structure of the hydrogel was maintained, although the surface area increased from 2.945 to 11.267 m^2/g as the amount of PEDOT:PSS increased from 0 to 1.8% (Fig. 3, E to H). The incorporation of external substances facilitates the formation of small pores within the hydrogel, increasing the overall surface area (*48*). More characterization data including images of the microstructure are shown in fig. S6.

Next, we characterized the electrical properties of the PEDOT:PSS/PAAm hydrogel with different concentrations of PEDOT:PSS. To

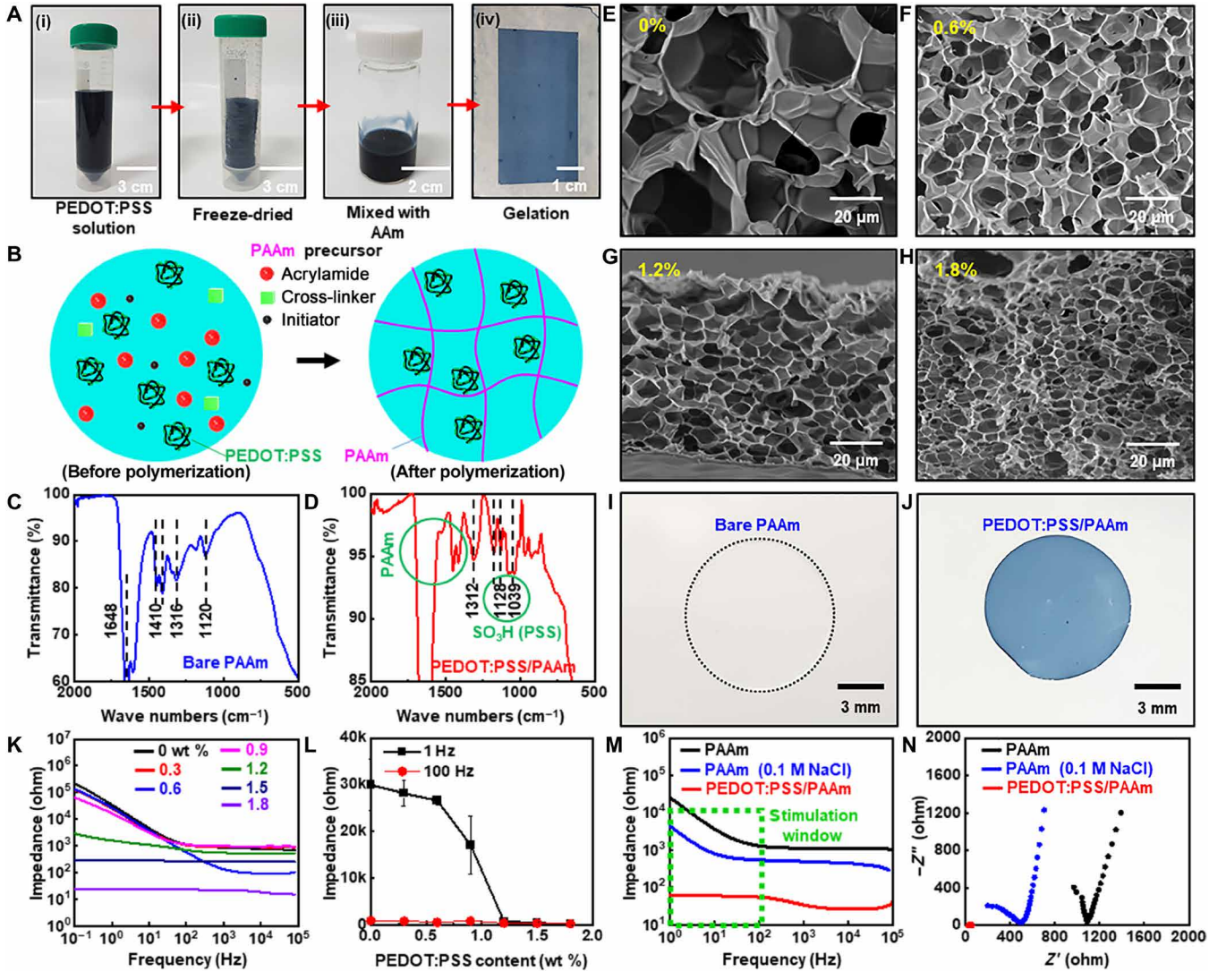

Fig. 3. Synthesis and characterization of the low-impedance hydrogel. (**A**) Fabrication process of the low-impedance hydrogel using PEDOT:PSS. (**B**) Illustration of the internal structure of the low-impedance hydrogel. (**C** and **D**) Fourier transform–IR (FT-IR) spectra of the bare PAAm hydrogel (C) and the PEDOT:PSS/PAAm hydrogel (D). (**E** to **H**) SEM images of the bare PAAm hydrogel (E) and the PEDOT:PSS/PAAm hydrogel (F to H). (**I** and **J**) Images of the laser-cut sample of the bare PAAm hydrogel (I) and the low-impedance hydrogel (J). (**K**) Bode plots of the hydrogels with various concentrations of PEDOT:PSS. (**L**) Impedance of hydrogels with various concentrations of PEDOT:PSS at 1 and 100 Hz. (**M** and **N**) Bode (M) and Nyquist (N) plots for the bare PAAm hydrogel, the PAAm hydrogel with 0.1 M NaCl, and the hydrogel with 1.8 wt % PEDOT:PSS. Photo credit: Yongseok Joseph Hong, Seoul National University.

control the size of the patterned hydrogel, the hydrogels were cut by a laser cutter (Fig. 3, I and J). Two patterned hydrogel films were prepared, and each hydrogel film was placed on a Pt electrode. Two sets of the Pt electrode with the hydrogel were stacked with the hydrogel sides facing each other, and the impedance of the hydrogel was measured with an electrochemical analyzer. As shown in Fig. 3K, impedance of the hydrogel tended to decrease as the amount of PEDOT:PSS increased, verifying the impedance lowering effect of PEDOT:PSS (*45*). In addition, impedance can be lowered by increasing the surface area of electrodes (*45*). Thus, the presence of PEDOT:PSS and the unique porous structure of the PEDOT:PSS/PAAm hydrogel contribute to the low impedance.

Given that a TENS typically operates in a frequency range of 1 to 100 Hz (*4*), we analyzed the impedance of hydrogels with various PEDOT:PSS concentrations at 1 and 100 Hz (Fig. 3L). At a low frequency (1 Hz), the impedance lowering effect of PEDOT:PSS was more prominent than at a high frequency (100 Hz). Compared with the bare hydrogel or hydrogel with ion salts (0.1 M NaCl), the PEDOT:PSS/PAAm hydrogel showed much lower impedance within 1 to 100 Hz (green dotted box in Fig. 3M). In addition, Nyquist plots confirmed that only the PEDOT:PSS/PAAm hydrogel maintained low resistance and reactance (Fig. 3N).

Wearable biosensors with the hydrogel interface for transcutaneous measurement of oxygen pressure and local impedance

We next applied the ultrathin, functionalized hydrogel to wearable biosensors. Figure 4A and insets show schematic illustrations of the

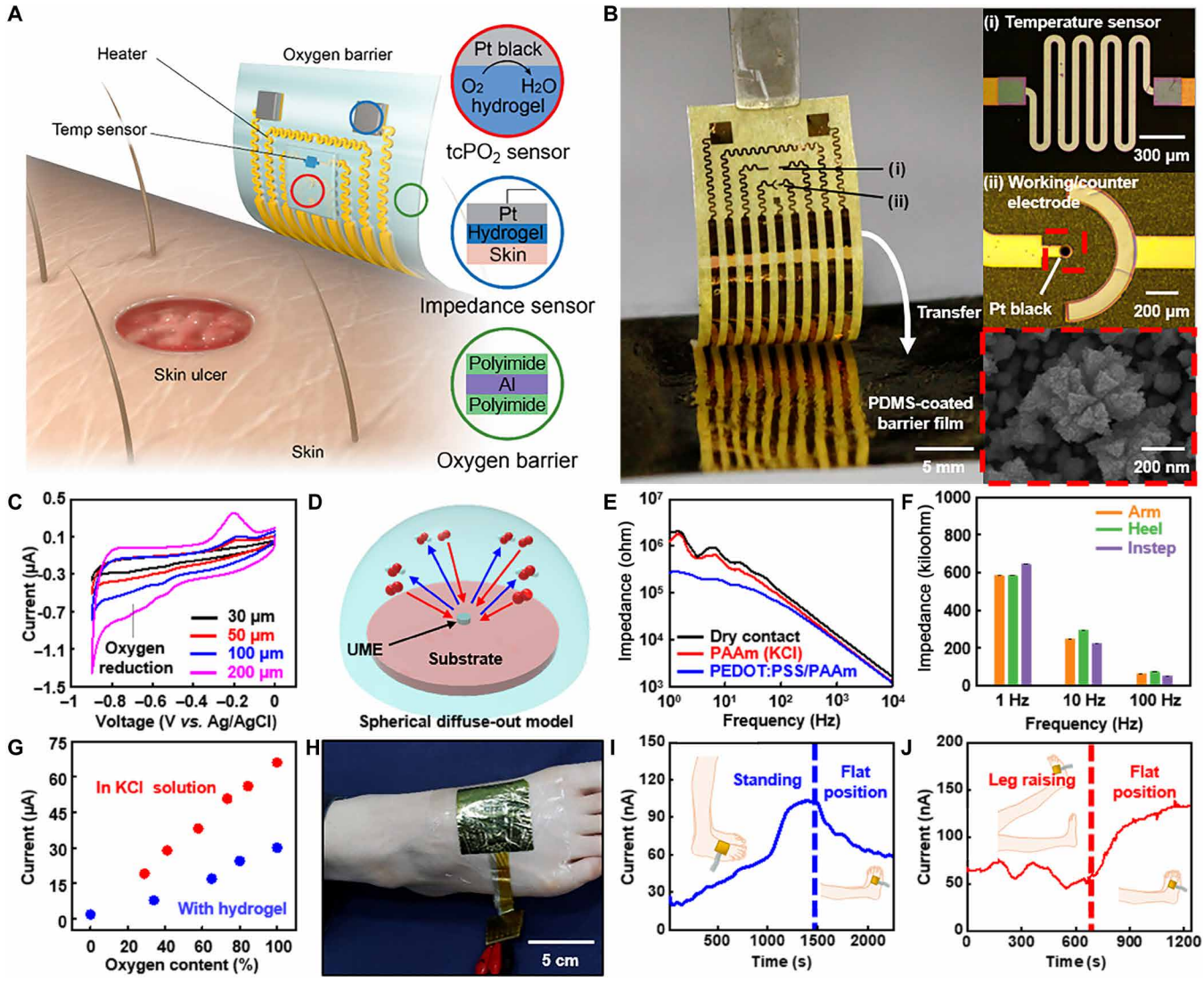

Fig. 4. Wearable transcutaneous biosensors for the measurement of $tcPO_2$ and local impedance. (**A** and **B**) Illustration (A) and a corresponding picture (B) of wearable transcutaneous biosensors for the measurement of $tcPO_2$ and local tissue impedance. PDMS, poly(dimethylsiloxane). (**C**) Cyclic voltammetry (CV) analysis of working electrodes with different dimensions. (**D**) Schematic illustration of the ultramicroelectrode (UME) concept. (**E**) Electrochemical impedance spectroscopy analysis of the tissue impedance using electrodes with different contacts. (**F**) Impedance at three different parts of the human body. (**G**) Calibration curves of an oxygen sensor with the liquid electrolyte and the hydrogel interface. (**H**) Image of the sensor attached on the foot for measuring $tcPO_2$ in vivo. (**I** and **J**) Results of in vivo $tcPO_2$ measurement for various leg positions; while the subject is standing (I, left), while the leg is at a flat position (I, right), and when a raised leg is moved back to the flat position (J). Photo credits: (B) Chanhyuk Lim, Seoul National University and (H) Yongseok Joseph Hong, Seoul National University.

$tcPO_2$ and local impedance sensors. The devices were encapsulated with a multilayered oxygen barrier film made of PI/Al/PI, which prohibits influx/efflux of oxygen between the device and the external environment (fig. S7) (*49*). In addition, the encapsulation layer prevents the hydrogel from its dehydration, thus maintaining the electrochemical performance of the hydrogel-electrode interface (fig. S8). The biosensors are pictured in Fig. 4B. A layer of Pt black was electrodeposited on a Pt thin film electrode (red dashed box in insets), and the resulting electrode has a 3D nanostructure that maximizes the electrochemically active surface area (fig. S9).

For $tcPO_2$ sensing, an electrochemical device with three electrodes, which consists of a working electrode (Pt black nanostructure), a counter electrode (Pt thin film), and a reference electrode (Ag/AgCl), was fabricated. Mild heating was applied to the skin through the hydrogel interface, extracting oxygen molecules from the blood vessels under the skin through the hydrogel interface to reach the device. The diffused oxygen is electrochemically reduced on the working electrode, measuring the reduction current. To avoid overheating, a temperature sensor was integrated. For local impedance sensing, a pair of Pt electrodes were used.

Cyclic voltammetry (CV) measurement showed an oxygen reduction peak near −0.7 V (Fig. 4C) (*50*). For reliable detection, the dimension of the working electrode was adjusted to be small, which results in a small oxygen reduction peak. This can be explained by

the diffusion behavior of substances near the working electrode depending on the electrode dimensions (*51*). In a large working electrode, substance diffusion follows a linear diffuse-out model. In contrast, when a small working electrode is adopted, substance diffusion follows a spherical diffuse-out model (Fig. 4D). Such adjustment of the peak current level is helpful for reliably measuring the oxygen reduction current due to the linear diffusion behavior of substances.

For in vivo evaluation of biosensor performance, local impedance was measured on the front of the forearm using a device with three types of electrodes, i.e., an electrode with a dry surface, a conventional ionic hydrogel (PAAm hydrogel with 0.1 M KCl), and a low-impedance hydrogel (PEDOT:PSS/PAAm hydrogel). The detailed procedure for the measurement of the local impedance was explained in Materials and Methods. The electrode with the PEDOT:PSS/PAAm hydrogel showed the lowest impedance, especially in the low frequency range ($<10^2$ Hz; Fig. 4E), which enables precise impedance sensing. In addition, local impedances were measured on the instep and the heel of the human foot with the low-impedance hydrogel electrode (fig. S10). The impedance values obtained on the three different parts of the human body were compared at 1, 10, and 100 Hz (Fig. 4F).

When $tcPO_2$ was measured in vivo, we found that the reduction current showed a linear correlation with the oxygen concentration, under both the liquid electrolyte (0.1 M KCl) and hydrogel (Fig. 4G) interface. Therefore, the amount of oxygen molecules extracted from the human skin can be estimated from the reduction current. The $tcPO_2$ sensor with the oxygen barrier film was attached to a human foot (Fig. 4H) to measure $tcPO_2$ under various leg positions (Fig. 4, I and J). First, the skin is gently warmed by the integrated heater for 10 to 15 min to extract oxygen. When the subject stood up, the blood flowed downward and the current gradually increased (Fig. 4I). When the leg was resting horizontally, the current slowly decreased. Meanwhile, the current slightly decreased and then rapidly increased when the leg was kept upright and then lowered (Fig. 4J). We repeated the in vivo $tcPO_2$ measurement. Similar tendencies for the relationship between the current and the leg positions could be observed (fig. S11). To enhance the accuracy of the in vivo $tcPO_2$ measurement, further improvements in the fabrication of electrodes and the measurement protocol as well as comparison to the commercial medical equipment should be done in the future. Thus, $tcPO_2$ sensor can monitor physiological changes such as the blood flow rate and the local amount of oxygen supplied to the tissue.

Wearable therapeutic devices with the hydrogel interface for transcutaneous drug delivery and electrical stimulation

Last, the ultrathin, functionalized hydrogel was integrated with a transcutaneous drug delivery device and TENS (Fig. 5, A and B). For drug delivery, iontophoresis is normally used (*52*); this consists of an electric field between two electrodes that drives the penetration of ionized drug molecules into the skin. Although an external power supply is typically used, a self-powered wearable device without a connection to a power supply was fabricated for point-of-care therapy. The galvanic reaction between the cathode (AgCl) and anode (Zn) generates a potential of ~1.08 V; the insets in Fig. 5B show the microstructure of the cathode and anode. As the target drugs (e.g., diltiazem hydrochloride) are positively charged, the drug-laden hydrogel film was integrated on the anode and a hydrogel film with 0.9% NaCl was integrated on the cathode. In the case of the TENS, the low-impedance hydrogel was integrated with Pt electrodes.

To evaluate the performance of the galvanic cell in the self-powered iontophoretic device, a galvanostatic discharge test was performed at an applied current of 200 μA for ~6700 s (Fig. 5C), which is sufficient for the complete delivery of the drug payload. The potential and current of the AgCl/Zn galvanic cell were also measured at various external resistances to obtain the output power of the galvanic cell (Fig. 5D); when the external resistance was 1 kiloohm, the maximum output power was 60 μW.

Drug delivery via iontophoresis was compared to the control (i.e., natural diffusion) using porcine skin (Fig. 5E). Rhodamine B molecules (model drug for easy visualization) delivered by the self-powered iontophoretic patch penetrated twice more deeply into the skin than that of control. The similar result was obtained in the iontophoretic delivery of rhodamine B molecules into the skin near the abdomen of a rat in vivo (fig. S12). Transdermal drug delivery was also verified in vivo (Fig. 5F), where local delivery of diltiazem chloride was conducted on 8-week-old male Sprague-Dawley (SD) rats. diltiazem chloride is a calcium channel blocker (*53*) that expands blood vessels and decreases heart rate. Thus, a three-lead electrocardiogram (ECG) was used to visualize drug delivery. The average R-R interval ($n = 4$) in the ECG (i.e., the time interval between heartbeats) increased from ~160 to ~195 ms during monitoring, indicating that the heart rate decreased from ~373 to ~307 beats per minute. Therefore, the results of the ECG confirm the successful delivery of diltiazem hydrochloride to the rat through the mass-permeable hydrogel.

For the TENS, the potential difference between two electrodes generates an electric current, which is delivered through the skin to stimulate peripheral nerves. The magnitude of the electric current depends on the applied potential difference. We tested the charge injections into porcine skin using various electrodes in vitro, including an electrode with a wet contact [deionized (DI) water], a hydrogel with ion salts (0.1 M KCl), and a PEDOT:PSS/PAAm hydrogel. Biphasic electrical pulses of 1 Hz (Fig. 5G), 10 Hz (Fig. 5H), and 100 Hz (Fig. 5I) were applied between the electrodes. The electrode with the PEDOT:PSS/PAAm hydrogel transmitted the largest amount of current at 1, 10, and 100 Hz (Fig. 5J), confirming its high-charge injection efficiency.

DISCUSSION

In the present study, we developed a tissue-like quasi-solid interface using an ultrathin, functionalized hydrogel. This ultrasoft hydrogel integrated wearable devices with the human skin seamlessly. Furthermore, the hydrogel featured a high mass-permeability for bioanalytes and drugs. We also formulated a PEDOT:PSS-based low-impedance hydrogel. The properties of the ultrathin, functionalized hydrogel were confirmed through theoretical analyses. To verify the utility of the proposed hydrogel interface, wearable bioelectronic devices with the hydrogel interface were developed for $tcPO_2$ sensing, impedance sensing, iontophoresis, and TENS. Through a series of experiments in vitro and in vivo, the performance of such devices for wearable diagnosis and therapy were demonstrated. Thus, this tissue-like hydrogel interface has a great potential for making various kinds of wearable bioelectronics a reality.

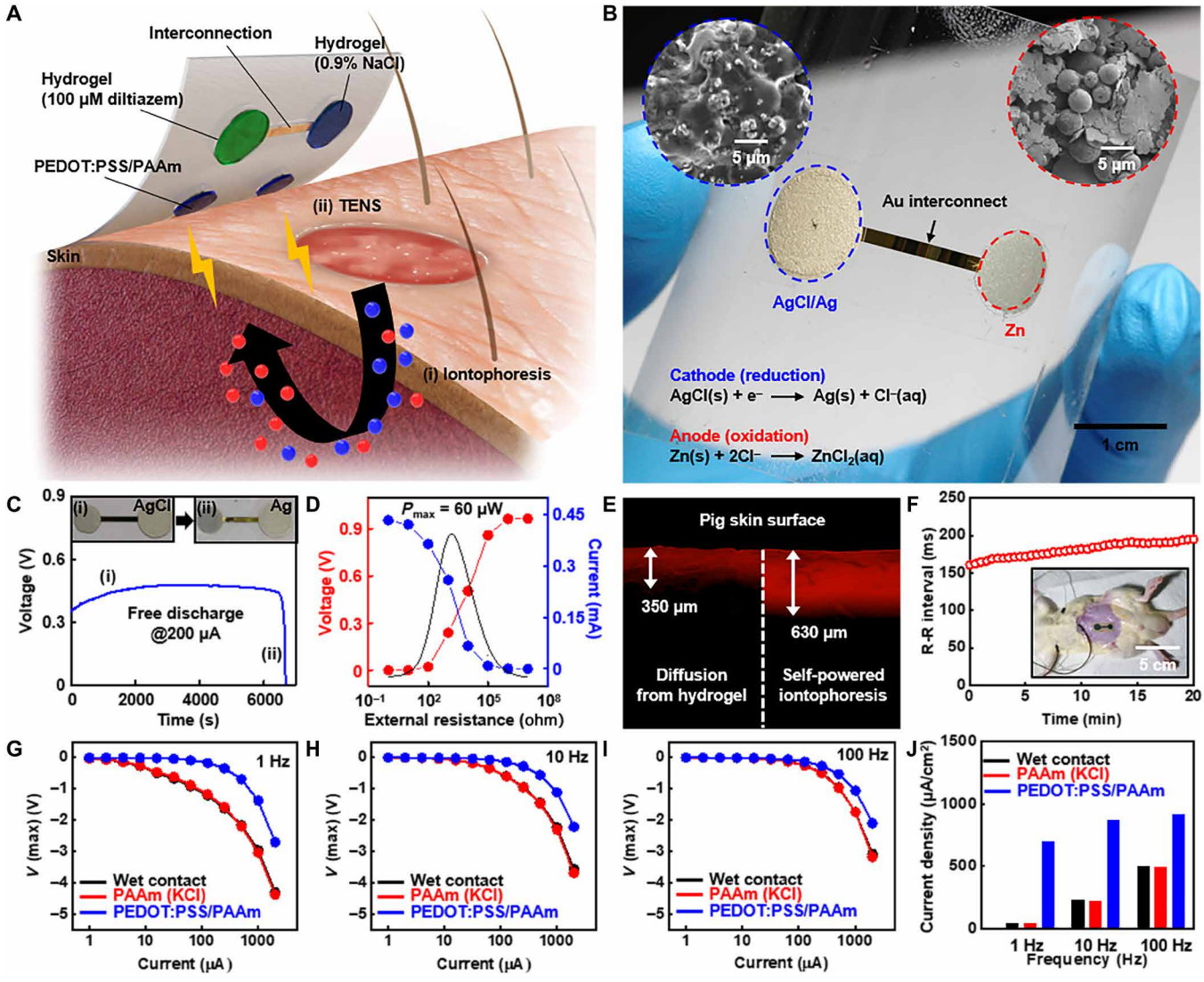

Fig. 5. Wearable therapeutic devices for transcutaneous drug delivery and electrical stimulation. (**A** and **B**) Illustration (A) and the corresponding picture (B) of the device for self-powered iontophoresis and TENS. Insets in (B) show the microstructure of the AgCl cathode and Zn anode. (**C**) Time-resolved discharge curve (under 200 μA) of a galvanic cell that consists of the AgCl cathode and Zn anode for self-powered iontophoresis. (**D**) Estimation of the maximum power of the galvanic cell. (**E**) In vitro drug delivery into porcine skin via natural diffusion and the self-powered iontophoretic patch (red, rhodamine B ions as a model drug for easy visualization). (**F**) Delivery of the drug (diltiazem hydrochloride) using the self-powered iontophoretic patch in vivo. The R-R interval was obtained via ECG measurement. Inset shows the self-powered iontophoretic patch attached to the abdomen of a Sprague-Dawley (SD) rat. (**G** to **I**) Charge injection test on porcine skin using electrodes with a wet contact, a PAAm hydrogel with 0.1 M KCl, and a PEDOT:PSS/PAAm hydrogel under 1 Hz (G), 10 Hz (H), and 100 Hz (I). (**J**) Maximum current injection at different frequencies for each type of electrode. Photo credits: (B) Chanhyuk Lim, Seoul National University and (F) Yongseok Joseph Hong, Seoul National University.

MATERIALS AND METHODS

Synthesis of mass-permeable and low-impedance PAAm hydrogels

For fabricating the mass-permeable PAAm hydrogel, 2.2 M AAm (A8887, Sigma-Aldrich, St. Louis, MO) aqueous solution, 0.06 weight % (wt %) *N*,*N*-methylenebisacrylamide (MBAA; M7279, Sigma-Aldrich), and 0.16 wt % APS (A0878, Samchun Chemicals, Seoul, Republic of Korea) were mixed and degassed. After adding 0.25 wt % *N*,*N*,*N*′,*N*′-tetramethylethylenediamine (T7024, Sigma-Aldrich), the mixture was poured into a custom-made mold with a space (thickness, 100 μm) and covered with a glass slide. Next, the mixture was allowed to polymerize by curing with ultraviolet light (Fusion Cure System, Minuta Technology, Osan, Republic of Korea) for 2 hours to produce ultrathin PAAm hydrogel films. The preparation of low-impedance PEDOT:PSS/PAAm hydrogel began with freeze-drying PEDOT:PSS solution (739332, Sigma-Aldrich). The solidified PEDOT:PSS was then dissolved in DI water and degassed. The degassed PEDOT:PSS solution was mixed with 0.5 ml of AAm/MBAA solution (A9926, Sigma-Aldrich) and 50 μl of 10 wt % APS solution. The mixed solution was poured into the mold and covered with a glass slide. Thermal polymerization was conducted on a hot plate at 90°C for 15 min to produce low-impedance PEDOT:PSS/PAAm hydrogel films. The hydrogel films were patterned with a laser cutter (VLS 2.30, Universal Laser Systems, Scottsdale, AZ) and stored in DI water until further use.

Characterization of mass-permeable and low-impedance hydrogels

The microstructure and chemical composition of freeze-dried PAAm hydrogels were assessed using SEM (S-3400N, Hitachi, Tokyo, Japan) and field emission SEM (MERLIN Compact, ZEISS, Oberkochen, Germany) equipped with an EDS. An FT-IR spectrometer (Nicolet iS50; Thermo Fischer Scientific, Waltham, MA) was used to confirm the complete polymerization of AAm into PAAm. The surface area of hydrogels was measured with a Brunauer-Emmett-Teller surface area analyzer (BELSORP-mini II, MicrotracBEL, Osaka, Japan). The diffusion of drug molecules through the PAAm hydrogel was demonstrated using rhodamine B dye (R6626, Sigma-Aldrich); a drop of 0.1% rhodamine B solution was placed onto a 1000-μm-thick film of PAAm hydrogel, and its diffusion depth was measured by confocal microscopy (LSM 780, Zeiss). The transfer of heat flux through PAAm hydrogel was characterized using an IR camera (ThermoVision A320, FLIR Systems, Wilsonville, OR); PAAm hydrogel films were placed onto a heating plate that was set to 43°C and their surface temperatures monitored. For the impedance measurement, two hydrogel films were patterned into a rectangular shape (1 cm by 2 cm) by a laser cutter. Next, each piece of the hydrogel film was placed on a Pt electrode (1 cm by 5 cm). Then, the sample was partially exposed (exposed area, 1 cm by 1 cm) and dried in a convection oven at 60°C for 10 min. For reswelling of the hydrogel film, 30 μl of DI water was dropped on the hydrogel film. Two sets of the Pt electrode with the hydrogel film were stacked with the hydrogel sides facing each other, and the impedance of the hydrogel film was measured with an electrochemical analyzer (CHI660E, CH Instruments, Austin, TX) in a frequency range of 10^{-1} to 10^{5} Hz.

Preparation of artificial skin

A negative skin replica was made out of a silicone rubber (Body Double, Smooth-On, Easton, PA). The skin replica was then treated with a mold release agent (Ease Release 200, Mann Release Technologies, Macungie, PA), after which another silicone rubber (Dragon Skin, Smooth-On) was applied. After curing, the cured Dragon Skin silicon rubber was detached from the negative skin replica. The surface of the artificial skin (Dragon Skin) was examined using SEM and a 3D laser scanning microscope (VK-X200K, Keyence, Osaka, Japan).

Fabrication and characterization of the $tcPO_2$ sensor

The oxygen barrier film for the $tcPO_2$ sensor was fabricated by stacking a PI layer (1.3 μm), Al film (300 nm), and PI layer (1.3 μm). The oxygen permeability of the oxygen barrier film was measured using an oxygen transmission rate analyzer (OX-TRAN 2/21 MD, MOCON, Minneapolis, MN). The PI layer was formed by spin coating poly(pyromellitic dianhydride-*co*-4-4′-oxydianiline), amic acid solution (575798, Sigma-Aldrich), and subsequent thermal imidization. Then, Cr/Au (7/70 nm) was deposited and patterned for Pt electrodeposition. A Pt thin film was deposited using an aqueous solution containing 0.1 M H_2PtCl_6 (C0641, Kojima Chemicals, Sayama, Japan) and 0.1 M KCl (P3911, Sigma-Aldrich) at −0.3 V for 30 s. Subsequently, a layer of Pt black was formed on the electrodeposited Pt electrode with an aqueous solution containing 0.1 M H_2PtCl_6 and 0.001 M lead acetate trihydrate (L33, Alfa Aesar, Haverhill, MA) at −0.2 V for 30 s. The extraneous parts of the Cr/Au film were etched away and an encapsulation layer of epoxy (SU-8 2002, Kayaku Advanced Materials, Westborough, MA) was formed. Last, the fabricated sensor was transferred onto a medical-grade flexible substrate (Tegaderm, 3M, Saint Paul, MN) using a water-soluble tape (Water-Soluble Wave Solder Tape 5414, 3M), after which the ultrathin PAAm hydrogel with 0.1 M KCl was placed onto the fabricated sensor. The electrochemical property of the Pt electrodes with different dimensions was compared using a CV method. A counter electrode of the Pt wire and a reference electrode of Ag/AgCl were used for the measurement. The CV curves were obtained in the 0.1 M KCl aqueous solution under a scan rate of 0.1 V s^{-1}.

Fabrication and characterization of the impedance sensor and TENS electrode

For the impedance sensor and TENS electrode, Pt electrodes were prepared and transferred onto a medical-grade flexible substrate in the same manner as the $tcPO_2$ sensor. For the TENS electrode, charge injection tests were performed on a porcine skin. Patterned hydrogel films covered both TENS electrodes connected to an electrochemical analyzer. A biphasic pulse was applied between the two electrodes with target currents of 1 to 2048 μA. The potential difference before, during, and after applying the biphasic pulse was monitored using the electrochemical analyzer. For data analysis, the potential difference before applying the biphasic current was subtracted from the peak potential difference.

Fabrication and characterization of the iontophoresis electrode

A dumbbell-shaped Cr/Au (7/70 nm) pattern was formed on a PI-coated SiO_2 wafer by thermal evaporation through a shadow mask. The cathode and anode regions of the iontophoresis device were defined with a patterned epoxy layer. The AgCl slurry (cathode) and Zn slurry (anode) were coated on the exposed part of Au electrodes. The AgCl slurry contains poly(vinylidene fluoride-*co*-hexafluoropropylene) (PVdF-HFP; Kynar 2801, Arkema, Colombes, France), AgCl nanoparticles, and Ag flakes (00783, Alfa Aesar) in a 1:7.9:1.1; the AgCl nanoparticle was synthesized via the chlorination of Ag nanopowder (45509, Alfa Aesar) in $FeCl_3$ (157740, Sigma-Aldrich) aqueous solution (200 mM). The Zn slurry contains PVdF-HFP, Zn powder (13789, Alfa Aesar), and Ag flakes in a 1:8:1 weight ratio. *N*-methyl-2-pyrrolidone was used as a solvent to make the slurries. Last, the fabricated iontophoresis device was transferred onto a medical-grade flexible substrate. The efficacy of the self-powered iontophoresis patch was assessed by monitoring the diffusion depth of rhodamine B dye molecules through porcine skin. As control, a film of PAAm hydrogel containing 0.1% rhodamine B was applied onto porcine skin. After diffusion for 20 min, the cross-sectional area was observed using an inverted fluorescence microscope (Eclipse Ti-S, Nikon, Tokyo, Japan). The same experiment was performed with 8-week-old male SD rats. The delivery of rhodamine B molecules into the abdomen of rats was measured by confocal microscopy (LSM 710, Zeiss, Germany).

Device demonstrations via in vivo experiments

All in vivo experiments on human subjects were performed under approval by the Institutional Review Board (IRB) of Seoul National University (IRB nos. 1605/003-003 and 2011/002-018). In vivo $tcPO_2$ monitoring was conducted on the instep of the foot after attaching the sensor to the skin using a pretaping spray (Tuffner Pre-Tape Spray, Mueller, Prairie du Sac, WI). The skin was preheated to 45°C, and the oxygen reduction current was monitored using an

electrochemical analyzer. For the in vivo measurement of the local impedance, devices with three different types of electrodes, i.e., a Pt electrode with a dry surface, a conventional ionic hydrogel (PAAm hydrogel with 0.1 M KCl), and a low-impedance hydrogel (PEDOT:PSS/PAAm hydrogel) were prepared. Two pieces of the hydrogel were patterned into 11-mm-diameter circles. Next, each hydrogel piece was placed on a Pt electrode with a circular opening area with a diameter of 1 cm and dried in a convection oven at 60°C for 10 min. The dried hydrogel pieces were reswollen by dropping 30 μl of DI water on each set of the hydrogel on the Pt electrode. Two sets of the Pt electrode with the hydrogel were placed on the forearm side by side with a central distance of 2 cm, and the local impedance was measured with an electrochemical analyzer in a frequency range of 10^0 to 10^4 Hz. In addition, the in vivo measurement of the local impedance was conducted on the instep and heel of the human foot with the low-impedance hydrogel electrode. The procedure for the tissue impedance measurement was the same as the above description. The local delivery of diltiazem hydrochloride (D3662, Tokyo Chemical Industry, Japan) was conducted on 8-week-old male SD rats. A PAAm hydrogel film (3% diltiazem hydrochloride + 0.9% NaCl) was placed on the Zn anode, while another PAAm hydrogel film (0.9% NaCl) was placed on the AgCl cathode of the iontophoretic device. The three-lead ECG of SD rats was recorded with a data acquisition device (PowerLab 8/35, ADInstruments, Sydney, Australia). During ECG measurement, the iontophoretic device was placed on a shaved abdominal region of SD rats and fixed with a medical-grade flexible film.

SUPPLEMENTARY MATERIALS

Supplementary material for this article is available at http://advances.sciencemag.org/cgi/content/full/7/19/eabd3716/DC1

REFERENCES AND NOTES

1. V. E. de Meijer, H. P. van't Sant, S. Spronk, F. J. Kusters, P. T. den Hoed, Reference value of transcutaneous oxygen measurement in diabetic patients compared with nondiabetic patients. *J. Vasc. Surg.* **48**, 382–388 (2008).
2. A. Kekonen, M. Bergelin, J. E. Eriksson, A. Vaalasti, H. Ylänen, J. Viik, Bioimpedance measurement based evaluation of wound healing. *Physiol. Meas.* **38**, 1373–1383 (2017).
3. B. Das Kurmi, P. Tekchandani, R. Paliwal, S. Rai Paliwal, Transdermal drug delivery: opportunities and challenges for controlled delivery of therapeutic agents using nanocarriers. *Curr. Drug Metab.* **18**, 481–495 (2017).
4. W. Gibson, B. M. Wand, N. E. O'Connell, Transcutaneous electrical nerve stimulation (TENS) for neuropathic pain in adults. *Cochrane Database Syst. Rev.* **9**, CD011976 (2017).
5. S. Park, S. W. Heo, W. Lee, D. Inoue, Z. Jiang, K. Yu, H. Jinno, D. Hashizume, M. Sekino, T. Yokota, K. Fukuda, K. Tajima, T. Someya, Self-powered ultra-flexible electronics via nano-grating-patterned organic photovoltaics. *Nature* **561**, 516–521 (2018).
6. D.-H. Kim, N. Lu, R. Ma, Y.-S. Kim, R.-H. Kim, S. Wang, J. Wu, S. M. Won, H. Tao, A. Islam, K. J. Yu, T.-I. Kim, R. Chowdhury, M. Ying, L. Xu, M. Li, H.-J. Chung, H. Keum, M. McCormick, P. Liu, Y.-W. Zhang, F. G. Omenetto, Y. Huang, T. Coleman, J. A. Rogers, Epidermal Electronics. *Science* **333**, 838–843 (2011).
7. C. Choi, M. K. Choi, S. Liu, M. S. Kim, O. K. Park, C. Im, J. Kim, X. Qin, G. J. Lee, K. W. Cho, M. Kim, E. Joh, J. Lee, D. Son, S.-H. Kwon, N. L. Jeon, Y. M. Song, N. Lu, D.-H. Kim, Human eye-inspired soft optoelectronic device using high-density MoS_2-graphene curved image sensor array. *Nat. Commun.* **8**, 1664 (2017).
8. K. Sim, S. Chen, Z. Li, Z. Rao, J. Liu, Y. Lu, S. Jang, F. Ershad, J. Chen, J. Xiao, C. Yu, Three-dimensional curvy electronics created using conformal additive stamp printing. *Nat. Electron.* **2**, 471–479 (2019).
9. M. Choi, Y. J. Park, B. K. Sharma, S.-R. Bae, S. Y. Kim, J.-H. Ahn, Flexible active-matrix organic light-emitting diode display enabled by MoS2 thin-film transistor. *Sci. Adv.* **4**, eaas8721 (2018).
10. W. Gao, S. Emaminejad, H. Y. Y. Nyein, S. Challa, K. Chen, A. Peck, H. M. Fahad, H. Ota, H. Shiraki, D. Kiriya, D.-H. Lien, G. A. Brooks, R. W. Davis, A. Javey, Fully integrated wearable sensor arrays for multiplexed in situ perspiration analysis. *Nature* **529**, 509–514 (2016).
11. H. Zhang, P. Gutruf, K. Meacham, M. C. Montana, X. Zhao, A. M. Chiarelli, A. Vázquez-Guardado, A. Norris, L. Lu, Q. Guo, C. Xu, Y. Wu, H. Zhao, X. Ning, W. Bai, I. Kandela, C. R. Haney, D. Chanda, R. W. Gereau IV, J. A. Rogers, Wireless, battery-free optoelectronic systems as subdermal implants for local tissue oximetry. *Sci. Adv.* **5**, eaaw0873 (2019).
12. S. Imani, A. J. Bandodkar, A. M. V. Mohan, R. Kumar, S. Yu, J. Wang, P. P. Mercier, A wearable chemical–electrophysiological hybrid biosensing system for real-time health and fitness monitoring. *Nat. Commun.* **7**, 11650 (2016).
13. E. Roh, H.-B. Lee, D.-I. Kim, N.-E. Lee, A solution-processable, omnidirectionally stretchable, and high-pressure-sensitive piezoresistive device. *Adv. Mater.* **29**, 1703004 (2017).
14. S. Gong, L. W. Yap, B. Zhu, Q. Zhai, Y. Liu, Q. Lyu, K. Wang, M. Yang, Y. Ling, D. T. H. Lai, F. Marzbanrad, W. Cheng, Local crack-programmed gold nanowire electronic skin tattoos for in-plane multisensor integration. *Adv. Mater.* **31**, 1903789 (2019).
15. X. Chen, Y. J. Park, M. Kang, S.-K. Kang, J. Koo, S. M. Shinde, J. Shin, S. Jeon, G. Park, Y. Yan, M. R. MacEwan, W. Z. Ray, K.-M. Lee, J. A. Rogers, J.-H. Ahn, CVD-grown monolayer MoS2 in bioabsorbable electronics and biosensors. *Nat. Commun.* **9**, 1690 (2018).
16. Y. R. Lee, T. Q. Trung, B.-U. Hwang, N.-E. Lee, A flexible artificial intrinsic-synaptic tactile sensory organ. *Nat. Commun.* **11**, 2753 (2020).
17. S. Niu, N. Matsuhisa, L. Beker, J. Li, S. Wang, J. Wang, Y. Jiang, X. Yan, Y. Yun, W. Burnett, A. S. Y. Poon, J. B.-H. Tok, X. Chen, Z. Bao, A wireless body area sensor network based on stretchable passive tags. *Nat. Electron.* **2**, 361–368 (2019).
18. W. Lee, S. Kobayashi, M. Nagase, Y. Jimbo, I. Saito, Y. Inoue, T. Yambe, M. Sekino, G. G. Malliaras, T. Yokota, M. Tanaka, T. Someya, Nonthrombogenic, stretchable, active multielectrode array for electroanatomical mapping. *Sci. Adv.* **4**, eaau2426 (2018).
19. Y. Yang, Y. Song, X. Bo, J. Min, O. S. Pak, L. Zhu, M. Wang, J. Tu, A. Kogan, H. Zhang, T. K. Hsiai, Z. Li, W. Gao, A laser-engraved wearable sensor for sensitive detection of uric acid and tyrosine in sweat. *Nat. Biotechnol.* **38**, 217–224 (2020).
20. T. Ha, J. Tran, S. Liu, H. Jang, H. Jeong, R. Mitbander, H. Huh, Y. Qiu, J. Duong, R. L. Wang, P. Wang, A. Tandon, J. Sirohi, N. Lu, A chest-laminated ultrathin and stretchable e-tattoo for the measurement of electrocardiogram, seismocardiogram, and cardiac time intervals. *Adv. Sci.* **6**, 1900290 (2019).
21. S. Yang, Y.-C. Chen, L. Nicolini, P. Pasupathy, J. Sacks, B. Su, R. Yang, D. Sanchez, Y.-F. Chang, P. Wang, D. Schnyer, D. Neikirk, N. Lu, "Cut-and-Paste" Manufacture of multiparametric epidermal sensor systems. *Adv. Mater.* **27**, 6423–6430 (2015).
22. H. Lee, T. K. Choi, Y. B. Lee, H. R. Cho, R. Ghaffari, L. Wang, H. J. Choi, T. D. Chung, N. Lu, T. Hyeon, S. H. Choi, D.-H. Kim, A graphene-based electrochemical device with thermoresponsive microneedles for diabetes monitoring and therapy. *Nat. Nanotechnol.* **11**, 566–572 (2016).
23. H. Lee, C. Song, Y. S. Hong, M. S. Kim, H. R. Cho, T. Kang, K. Shin, S. H. Choi, T. Hyeon, D.-H. Kim, Wearable/disposable sweat-based glucose monitoring device with multistage transdermal drug delivery module. *Sci. Adv.* **3**, e1601314 (2017).
24. Y. Zhang, A. D. Mickle, P. Gutruf, L. A. M. Ilvried, H. Guo, Y. Wu, J. P. Golden, Y. Xue, J. G. Grajales-Reyes, X. Wang, S. Krishnan, Y. Xie, D. Peng, C.-J. Su, F. Zhang, J. T. Reeder, S. K. Vogt, Y. Huang, J. A. Rogers, R. W. Gereau IV, Battery-free, fully implantable optofluidic cuff system for wireless optogenetic and pharmacological neuromodulation of peripheral nerves. *Sci. Adv.* **5**, eaaw5296 (2019).
25. D. Son, J. Lee, S. Qiao, R. Ghaffari, J. Kim, J. E. Lee, C. Song, S. J. Kim, D. J. Lee, S. W. Jun, S. Yang, M. Park, J. Shin, K. Do, M. Lee, K. Kang, C. S. Hwang, N. Lu, T. Hyeon, D.-H. Kim, Multifunctional wearable devices for diagnosis and therapy of movement disorders. *Nat. Nanotechnol.* **9**, 397–404 (2014).
26. Y. Ling, T. An, L. W. Yap, B. Zhu, S. Gong, W. Cheng, Disruptive, soft, wearable sensors. *Adv. Mater.* **32**, 1904664 (2020).
27. W.-H. Yeo, Y.-S. Kim, J. Lee, A. Ameen, L. Shi, M. Li, S. Wang, R. Ma, S. H. Jin, Z. Kang, Y. Huang, J. A. Rogers, Multifunctional epidermal electronics printed directly onto the skin. *Adv. Mater.* **25**, 2773–2778 (2013).
28. S. Choi, S. I. Han, D. Jung, H. J. Hwang, C. Lim, S. Bae, O. K. Park, C. M. Tschabrunn, M. Lee, S. Y. Bae, J. W. Yu, J. H. Ryu, S.-W. Lee, K. Park, P. M. Kang, W. B. Lee, R. Nezafat, T. Hyeon, D.-H. Kim, Highly conductive, stretchable and biocompatible Ag–Au core–sheath nanowire composite for wearable and implantable bioelectronics. *Nat. Nanotechnol.* **13**, 1048–1056 (2018).
29. J. Lee, H. R. Cho, G. D. Cha, H. Seo, S. Lee, C.-K. Park, J. W. Kim, S. Qiao, L. Wang, D. Kang, T. Kang, T. Ichikawa, J. Kim, H. Lee, W. Lee, S. Kim, S.-T. Lee, N. Lu, T. Hyeon, S. H. Choi, D.-H. Kim, Flexible, sticky, and biodegradable wireless device for drug delivery to brain tumors. *Nat. Commun.* **10**, 5205 (2019).
30. X. P. Morelle, W. R. Illeperuma, K. Tian, R. Bai, Z. Suo, J. J. Vlassak, Highly stretchable and tough hydrogels below water freezing temperature. *Adv. Mater.* **30**, 1801541 (2018).
31. C.-C. Kim, H.-H. Lee, K. H. Oh, J.-Y. Sun, Highly stretchable, transparent ionic touch panel. *Science* **353**, 682–687 (2016).
32. H. Yuk, C. E. Varela, C. S. Nabzdyk, X. Mao, R. F. Padera, E. T. Roche, X. Zhao, Dry double-sided tape for adhesion of wet tissues and devices. *Nature* **575**, 169–174 (2019).
33. Y. Liu, J. Liu, S. Chen, T. Lei, Y. Kim, S. Niu, H. Wang, X. Wang, A. M. Foudeh, J. B.-H. Tok, Z. Bao, Soft and elastic hydrogel-based microelectronics for localized low-voltage neuromodulation. *Nat. Biomed. Eng.* **3**, 58–68 (2019).

34. J. Li, A. D. Celiz, J. Yang, Q. Yang, I. Wamala, W. Whyte, B. R. Seo, N. V. Vasilyev, J. J. Vlassak, Z. Suo, D. J. Mooney, Tough adhesives for diverse wet surfaces. *Science* **357**, 378–381 (2017).
35. C. Xie, X. Wang, H. He, Y. Ding, X. Lu, Mussel-inspired hydrogels for self-adhesive bioelectronics. *Adv. Funct. Mater.* **30**, 1909954 (2020).
36. H. Yuk, B. Lu, X. Zhao, Hydrogel bioelectronics. *Chem. Soc. Rev.* **48**, 1642–1667 (2019).
37. J. H. Koo, S. Jeong, H. J. Shim, D. Son, J. Kim, D. C. Kim, S. Choi, J.-I. Hong, D.-H. Kim, Wearable electrocardiogram monitor using carbon nanotube electronics and color-tunable organic light-emitting diodes. *ACS Nano* **11**, 10032–10041 (2017).
38. K. Sim, Z. Rao, Z. Zou, F. Ershad, J. Lei, A. Thukral, J. Chen, Q.-A. Huang, J. Xiao, C. Yu, Metal oxide semiconductor nanomembrane–based soft unnoticeable multifunctional electronics for wearable human-machine interfaces. *Sci. Adv.* **5**, eaav9653 (2019).
39. C. Lim, Y. Shin, J. Jung, J. H. Kim, S. Lee, D.-H. Kim, Stretchable conductive nanocomposite based on alginate hydrogel and silver nanowires for wearable electronics. *APL Mater.* **7**, 031502 (2019).
40. Y.-L. Shen, in *Constrained Deformation of Materials* (Springer, Boston, ed. 1, 2010), pp. 47.
41. M. Pawlaczyk, M. Lelonkiewicz, M. Wieczorowski, Age-dependent biomechanical properties of the skin. *Adv. Dermatol. Allergol.* **5**, 302–306 (2013).
42. T. Shay, O. D. Velev, M. D. Dickey, Soft electrodes combining hydrogel and liquid metal. *Soft Matter* **14**, 3296–3303 (2018).
43. L. Pan, F. Wang, Y. Cheng, W. R. Leow, Y.-W. Zhang, M. Wang, P. Cai, B. Ji, D. Li, X. Chen, A supertough electro-tendon based on spider silk composites. *Nat. Commun.* **11**, 1332 (2020).
44. Y. Wang, C. Zhu, R. Pfattner, H. Yan, L. Jin, S. Chen, F. Molina-Lopez, F. Lissel, J. Liu, N. I. Rabiah, Z. Chen, J. W. Chung, C. Linder, M. F. Toney, B. Murmann, Z. Bao, A highly stretchable, transparent, and conductive polymer. *Sci. Adv.* **3**, e1602076 (2017).
45. Y. Qiang, P. Artoni, K. J. Seo, S. Culaclii, V. Hogan, X. Zhao, Y. Zhong, X. Han, P.-M. Wang, Y.-K. Lo, Y. Li, H. A. Patel, Y. Huang, A. Sambangi, J. S. V. Chu, W. Liu, M. Fagiolini, H. Fang, Transparent arrays of bilayer-nanomesh microelectrodes for simultaneous electrophysiology and two-photon imaging in the brain. *Sci. Adv.* **4**, eaat0626 (2018).
46. V. R. Feig, H. Tran, M. Lee, Z. Bao, Mechanically tunable conductive interpenetrating network hydrogels that mimic the elastic moduli of biological tissue. *Nat. Commun.* **9**, 2740 (2018).
47. P. Sakunpongpitiporn, K. Phasuksom, N. Paradee, A. Sirivat, Facile synthesis of highly conductive PEDOT:PSSviasurfactant templates. *RSC Adv.* **9**, 6363–6378 (2019).
48. C. Martín, S. Merino, J. M. González-Domínguez, R. Rauti, L. Ballerini, M. Prato, E. Vázquez, Graphene improves the biocompatibility of polyacrylamide hydrogels: 3D polymeric scaffolds for neuronal growth. *Sci. Rep.* **7**, 10942 (2017).
49. S. Hong, J. Lee, K. Do, M. Lee, J. H. Kim, S. Lee, D.-H. Kim, Stretchable electrode based on laterally combed carbon nanotubes for wearable energy harvesting and storage devices. *Adv. Funct. Mater.* **27**, 1704353 (2017).
50. S. Iguchi, K. Mitsubayashi, T. Uehara, M. Ogawa, A wearable oxygen sensor for transcutaneous blood gas monitoring at the conjunctiva. *Sens. Actuators B Chem.* **108**, 733–737 (2005).
51. R. M. Wightman, Microvoltammetric electrodes. *Anal. Chem.* **53**, 1125A–1134A (1981).
52. M. R. Prausnitz, R. Langer, Transdermal drug delivery. *Nat. Biotechnol.* **26**, 1261–1268 (2008).
53. B. S. Bachenheimer, *Manual for Pharmacy Technicians* (American Society of Health System, ed. 5, 2019).
54. R. Quey, P. R. Dawson, F. Barbe, Large-scale 3D random polycrystals for the finite element method: Generation, meshing and remeshing. *Comput. Methods Appl. Mech. Eng.* **200**, 1729–1745 (2011).
55. W. Xing et al., in *Rotating Electrode Methods and Oxygen Reduction Electrocatalysts*. W. Xing, G. Yin, J. Zhang, Eds. (Elsevier Science, 2014), pp. 1–31.
56. P. O. Gendron, F. Avaltroni, K. J. Wilkinson, Diffusion coefficients of several rhodamine derivatives as determined by pulsed field gradient–nuclear magnetic resonance and fluorescence correlation spectroscopy. *J. Fluoresc.* **18**, 1093–1101 (2008).
57. B. F. Beck, *Karst Geohazards: Engineering and Environmental Problems in Karst Terrane* (A. A. Balkema, 1995).
58. ITIS Foundation, itis.swiss/virtual-population/tissue-properties/database/thermal-conductivity/.
59. S. Lee, J. Ha, H. Cheng, J. W. Lee, T. S. Jang, Y.-G. Jung, Y. Huang, J. A. Rogers, U. Paik, Surface-coverage-dependent cycle stability of core-shell nanostructured electrodes for use in lithium ion batteries. *Adv. Energy Mater.* **4**, 1300472 (2014).

Acknowledgments: All procedures were approved by the Institutional Animal Care and Use Committee (IACUC) of the Biomedical Research Institute of Seoul National University Hospital and Institutional Review Board of Seoul National University (SNUIRB). All experiments were performed according to IACUC and SNUIRB guidelines. **Funding:** This work was supported by IBS-R006-D1, IBS-R006-A1, and the National Research Foundation of Korea (NRF) grant funded by the Korean government (MSIT) (grant no. 2019R1A5A6099595). Y.J.H. acknowledges NRF grant funded by the Korean Government (NRF-2017H1A2A1043976-Global Ph.D. Fellowship Program). **Author contributions:** C.L., S.L., and D.-H.K. designed the experiments. C.L., Y.J.H., Y.S., S.B., and S.L. performed the experiments and analysis. J.J. and J.H.K. designed the hydrogel simulation model, performed simulations, and wrote simulation-related section. Y.J.H., S.-H.S., O.K.P., and S.H.C. performed animal experiments. C.L., S.L., T.H., and D.-H.K. wrote the paper. **Competing interests:** The authors declare that they have no competing interests. **Data and materials availability:** All data needed to evaluate the conclusions in the paper are present in the paper and/or the Supplementary Materials. Additional data related to this paper may be requested from the authors.

Submitted 16 July 2020
Accepted 19 March 2021
Published 7 May 2021
10.1126/sciadv.abd3716

Citation: C. Lim, Y. J. Hong, J. Jung, Y. Shin, S.-H. Sunwoo, S. Baik, O. K. Park, S. H. Choi, T. Hyeon, J. H. Kim, S. Lee, D.-H. Kim, Tissue-like skin-device interface for wearable bioelectronics by using ultrasoft, mass-permeable, and low-impedance hydrogels. *Sci. Adv.* **7**, eabd3716 (2021).